Surpassing the physical Nyquist limit to produce super-resolution cryo-EM reconstructions

J. Ryan Feathers[1], Katherine A. Spoth[2], and J. Christopher Fromme[1]

[1]Department of Molecular Biology and Genetics, Weill Institute for Cell and Molecular Biology, Cornell University, Ithaca, NY 14853 USA

[2]Cornell Center for Materials Research, Cornell University, Ithaca, NY 14853 USA

correspondence to J.C.F.: jcf14@cornell.edu

Abstract

Recent advances in single-particle cryo-electron microscopy (cryo-EM) methods have led to the determination of hundreds of high-resolution (< 4.0 Å) macromolecular structures. However, access to high-end instrumentation can be scarce and expensive. The resolution of cryo-EM reconstructions is fundamentally limited by the Nyquist frequency, which is half the sampling frequency of the detector and depends upon the magnification used. In principle, super-resolution imaging should enable reconstructions to surpass the physical Nyquist limit by increasing sampling frequency, yet there are no reports of reconstructions that do so. Here we report the use of super-resolution imaging with the K3 direct electron detector to produce super-resolution cryo-EM reconstructions significantly surpassing the physical Nyquist limit. We demonstrate that super-resolution imaging can be used to capture high-resolution information at lower magnifications, facilitating the imaging of thousands of particles per micrograph and maximizing the use of limited instrument time. Remarkably, using this approach we produced a 3.7 Å reconstruction of jack bean urease with particles selected from a single micrograph.

Introduction

The use of single-particle cryo-electron microscopy (cryo-EM) as a structural biology technique has gained wide adoption in recent years, in large part due to the development of direct electron detectors and advances in computational methods (Cheng et al., 2015; Cheng, 2015; Nogales and Scheres, 2015; Cheng et al., 2016). Dozens of institutions worldwide have acquired the sophisticated EM tools required to collect high-resolution data for determining the atomic structures of macromolecules using single-particle analysis techniques. Due to the high cost of acquisition and maintenance of these tools, as well as high demand for their use, there are strong incentives to maximize the amount of data collected per unit time.

A typical 24-hour experiment on a high-resolution EM instrument involves ~4-8 hours of setup time and ~16-20 hours of data collection time, resulting in hundreds or thousands of image exposures. A key decision made by the experimenter is the magnification used for imaging. The magnification needs to be large enough to capture high-resolution information. However, the higher the magnification used, the fewer particle images that are captured per micrograph, and therefore the smaller the dataset that will be collected in the same time period.

The resolution of cryo-EM reconstructions is fundamentally limited to the Nyquist frequency, which is half the sampling frequency of the detector. For example, if data is collected using a magnification which produces an image on the detector such that each 1.5 Å of the sample spans one pixel of the detector (image “pixel size” = 1.5 Å), then the Nyquist frequency is 1/3 $Å^{-1}$ and the maximum achievable resolution of the reconstruction (“Nyquist limit”) is 3.0 Å. The achievable resolution is further constrained by aliasing. Aliasing arises when an image projected onto a detector contains information at higher resolution (frequencies) than the Nyquist limit. This leads to artifacts in the image that can limit the achievable resolution.

The advent of direct electron detectors for cryo-EM experiments and advances in data processing have resulted in a “revolution” of hundreds of new high-resolution

macromolecular structures. These detectors can count individual electrons, greatly improving signal-to-noise (Bammes et al., 2012; Li et al., 2013b; McMullan et al., 2014; Ruskin et al., 2013; Cheng et al., 2016; Mendez et al., 2019). Fast readout rates enable exposures to be collected as movies which can be processed to correct for image blurring caused by sample motion. This motion correction results in a significant improvement in the information content at high resolution (Campbell et al., 2012; Li et al., 2013a).

Some direct electron detectors, such as the Gatan K2 and K3, can also generate "super-resolution" images. The super-resolution method takes advantage of the fact that a single electron is detected simultaneously by multiple adjacent pixels. The centroid of the electron can therefore be attributed to one quadrant of a physical pixel, resulting in a four-fold increase in the number of image pixels compared to physical detector pixels (Booth, 2012; Li et al., 2013b). At a given magnification, super-resolution data acquisition should reduce the effects of aliasing by effectively doubling the spatial sampling frequency.

In principle, super-resolution imaging should enable the resolution of cryo-EM reconstructions to surpass the physical Nyquist limit, and to approach what we term the "super-Nyquist" limit defined as half the sampling frequency of the super-resolution image. Indeed, super-resolution phase information was detectible in images collected on 2D protein crystals (Chiu et al., 2015). However, no 3D reconstructions with resolutions surpassing the physical Nyquist limit have been reported in the literature. In fact, the standard practice in the field is to either "bin" super-resolution pixels 2-fold to reduce the effects of aliasing while maintaining the physical pixel size in the binned images, or to avoid using super-resolution imaging at all.

Here we report the use of super-resolution imaging on the K3 direct electron detector to produce super-resolution cryo-EM reconstructions that surpass the physical Nyquist limit by as much as 1.4-fold. With a physical pixel size of 1.66 Å we obtained a 2.77 Å reconstruction and with a physical pixel size of 2.10 Å we obtained a 3.06 Å

reconstruction. We show that super-resolution imaging at lower magnifications enables collection of significantly larger datasets that retain high-resolution information. Therefore, very large datasets can be collected in modest timeframes, and standard-sized datasets can be collected in very short timeframes. As a proof of principle, we use this lower-magnification super-resolution (LMSR) imaging approach to generate a 3.72 Å reconstruction of jack bean urease using only a single exposure.

Results

Typical high-resolution single-particle cryo-EM experiments utilize physical pixel sizes of approximately 1.0 Å. For a typical medium-sized sample with dense particle distribution, this might result in ~400 particles per micrograph, and 500 exposures will result in a dataset with ~200,000 particles (Table 1). Samples are typically imaged after being applied to grids coated with a foil substrate consisting of an array of ~1-2 μm holes, with a single exposure taken per hole (alternative data collection strategies are addressed in the Discussion). The result is that most of the particles present in a hole are not actually imaged. Using a lower magnification results in more particles per exposure and therefore per dataset (Fig. 1A and Table 1), but reduces the maximum achievable resolution by increasing the physical pixel size of the image. The physical Nyquist limit has therefore constrained researchers to collect smaller datasets in order to reach a resolution at which reconstructions can be interpreted to build atomic molecular models *de novo*.

To assess the performance of the K3 direct electron detector operating in super-resolution mode, we determined its modulation transfer function (MTF), noise power spectrum (NPS), and detective quantum efficiency (DQE) using FindDQE (Ruskin et al., 2013) (Fig. 1B-D). We performed all measurements and experiments using a Talos Arctica operating at 200 kV with the K3 mounted on an imaging filter. We tested a range of dose-rates (20-40 e^-/physical pixel/second) and analyzed super-resolution images. The curves are similar overall to those reported for the K2, with significant DQE observed in the super-resolution frequency range (Li et al., 2013a; Ruskin et al., 2013;

McMullan et al., 2014). However, based on the NPS and DQE curves, the K3 appears to have less coincidence loss overall, maintains low coincidence loss at higher dose-rates, and has significantly higher DQE at low frequencies. These properties all likely result from the faster read-out rate of the K3 compared to the K2. Interestingly, there appears to be a trade-off between coincidence loss and signal-to-noise: at a dose rate of 20 e^-/physical pixel/second there appears to be less coincidence loss but also lower DQE(0) compared to a dose rate of 40 e^-/physical pixel/second.

To determine whether super-resolution imaging can be used to capture high-resolution information, we decided to use a magnification at which a reconstruction using physical pixels would be constrained by the physical Nyquist limit. We therefore imaged jack bean urease frozen in vitreous ice with a nominal magnification of 49,000x, resulting in a physical pixel size of 1.66 Å. Although the structure of this protein has been determined by X-ray crystallography (Balasubramanian and Ponnuraj, 2010), no EM reconstruction has been reported. Due to the lower magnification and fairly dense particle distribution, each micrograph contained ~1,700 particles. (Fig. 2A).

We used Serial-EM software (Mastronarde, 2005; Schorb et al., 2019) to automatically collect 240 super-resolution exposures. We did not subsequently bin the super-resolution micrographs, therefore the image pixel size used in data processing was 0.83 Å. Relion 3.0 software (Zivanov et al., 2018) was used for all data processing steps, including wrappers to MotionCor2 (Zheng et al., 2017) for motion correction and dose-weighting of movies and to GCTF (Zhang, 2016) for initial per-micrograph defocus estimation. To generate a 3D reference for template-based autopicking, we first performed 3D refinement with a small subset of the data, using a 60 Å low-pass filtered crystal structure of urease (Balasubramanian and Ponnuraj, 2010) as an initial reference model. Autopicking using this 3D template yielded ~359,000 particles from the entire dataset. Particle images were first extracted using a 2x-binned pixel size of 1.66 Å, equivalent to the physical pixel size, and 3D-refinement of the entire particle set resulted in a 3D reconstruction with a masked 0.143 Fourier-shell correlation (FSC)

resolution (Rosenthal and Henderson, 2003) that reached the physical Nyquist limit of 3.32 Å without any additional processing (see Figure S1 for FSC curve).

Particle images were then re-extracted using the unbinned super-resolution pixel size of 0.83 Å. Several rounds of 3D refinement interspersed with per-particle CTF refinement, Bayesian particle polishing, beam-tilt estimation (Zivanov et al., 2018, 2019), and 3D-classification produced a final subset of ~56,000 particles generating a 3D reconstruction with a masked 0.143 FSC resolution of 2.77 Å (Figs. 2B,C, S1, and Table 2). We note that using a 0.5 FSC cutoff, the resolution was 3.0 Å, and the electron density map showed clear side-chain densities consistent with a ~2.8 Å reconstruction (Fig. 2D). To assess the suitability of the reconstruction for atomic model refinement we manually modified the X-ray crystallographic atomic model of urease to fit the sharpened map and performed real-space refinement (Afonine et al., 2018b), producing a refined atomic model with excellent geometry and a model-map 0.5 FSC of 2.9 Å (Fig. 2D and Table 3). The sharpened map was of sufficient quality to enable *de novo* atomic model building. In fact, virtually all of the protein backbone and more than half of the sidechains were automatically modeled correctly using the automated "map-to-model" procedure (Terwilliger et al., 2018) within the Phenix software package (Adams et al., 2010) (Table 3). Therefore, by all criteria, the resolution of this 3D reconstruction surpassed the physical Nyquist limit. To our knowledge this represents the first reported example of a super-resolution cryo-EM reconstruction.

To determine if even lower magnifications could be used to obtain high-resolution reconstructions, we collected another dataset on the same sample at a nominal magnification of 39,000x, with a physical pixel size of 2.10 Å (Fig. 3A). We collected 284 super-resolution movie exposures and autopicked ~973,000 particles, with most images containing ~3500-3900 particles. 2D-classification (Fig. 3B) was used to remove ~128,000 "junk" particles. The remainder of the data processing procedure was similar to that described above (Fig. S2), resulting in a reconstruction with a masked resolution of 3.06 Å at the 0.143 FSC cutoff (3.30 Å at 0.5 FSC cutoff) using ~110,000 particles (Fig. 3C,D and Table 2). Again, the electron density map quality was consistent with this

resolution value (Fig. 3E) and suitable for *de novo* model building (Table 3), confirming that the physical Nyquist limit of 4.20 Å was significantly surpassed.

We considered the fact that ~110,000 is a rather large number of particles for reconstruction of a molecule with D3 (6-fold) symmetry. Additional 3D-classification to obtain a smaller subset of particles resulted in a 3.19 Å reconstruction using ~47,000 particles (data not shown). In contrast, as described above we used a slightly higher magnification to produce a 2.8 Å resolution reconstruction of the same sample (although a different sample grid was imaged) with ~56,000 particles. Taken together, these results suggest that these ~3.1 - 3.2 Å reconstructions using a 2.1 Å physical pixel size have reached the practical information limit imposed by the diminishing DQE of the detector beyond the physical Nyquist limit (Fig. 1D). We therefore conclude that super-resolution imaging with the K3 can be used to obtain reconstructions with resolutions reaching ~4/3 the physical Nyquist frequency limit with reasonable particle numbers.

Given the very large numbers of particles obtained per image at this magnification, we were curious to determine the smallest number of exposures that were required to produce a useful 3D-reconstruction. Using the same 39,000x magnification dataset, we reprocessed the data using smaller numbers of images. Importantly, we did not select the best particle subsets from the refined larger dataset, or select the best subset of micrographs. Instead we simply used the first exposures we collected and repeated the data processing procedure beginning with particle autopicking. We processed datasets with sizes of 20 and 5 micrographs. Surprisingly, both of these datasets resulted in 3D-reconstructions with masked 0.143 FSC resolutions, 3.34 Å and 3.60 Å, surpassing the physical Nyquist limit (Table 2).

We then chose two individual micrographs, selecting from among the first twenty those with the lowest estimated defocus values (0.8 and 0.9 μm) that also displayed good contrast. We processed each of these single micrographs as an independent dataset. Particles from one micrograph (0.8 μm defocus) generated a 3D-reconstruction with a masked 0.143 FSC resolution of 4.12 Å, while particles from the other micrograph

(0.9 μm defocus, Fig. 3A) generated a 3D-reconstruction with a masked 0.143 FSC resolution of 3.84 Å (Figs. 4A,B,C, S3, and Tables 2 and 3). We then selected three more individual micrographs from the larger 39,000x magnification dataset to process as independent datasets, and each of these produced 3D-reconstructions with similar masked 0.143 FSC resolutions: 4.05 Å, 3.98 Å, and 3.72 Å (Fig. 4B and Table 2). Remarkably, these five individual micrographs each resulted in a 3D-reconstruction that surpassed the physical Nyquist limit of 4.20 Å, although only three out of the five did so convincingly (Fig. 4B).

There are likely two aspects of the LMSR approach that enabled the production of super-resolution reconstructions from single image exposures on a 2-condenser-lens 200kV instrument. First, due to the low magnification and large size of the K3 sensor, up to ~3900 particles were present in each image, and ~2100-3200 of these were used in each of the final reconstructions (Table 2). These particle numbers are sufficient to generate high-resolution (< 4 Å) reconstructions because of the D3 (6-fold) symmetry of jack bean urease. Second, the particles appear to be positioned across a ~0.2 μm range of defocus distances in the image (Fig. 4D), perhaps due to the local topography of the ice layer in the hole (Fig. 4E). Single-particle experiments require particles to be imaged at varying defocus distances in order to compensate for the information loss ("zeros") at certain frequencies due to modulation of the image by the contrast transfer function (CTF) of the instrument. Typically, this is compensated for by acquiring exposures at different defocus distances during data collection. Our results demonstrate that the distribution of particle defocus distances in a single lower magnification image can be sufficient to overcome the information lost through CTF zeros. Defocus could also be deliberately varied in a single image through a small amount of stage tilt. For example, a 10° stage tilt would generate a 0.2 μm defocus range across the image field of view at this magnification.

Discussion

The best resolution achievable for a single-particle reconstruction of a macromolecule depends upon many factors, including the properties of the molecule itself, sample preparation quality, and the microscope imaging conditions. The LMSR method reported here uses super-resolution imaging to greatly increase the amount of high-resolution data that can be collected with limited instrument time. There are two main benefits of the LMSR approach. The first is the ability to collect several million particle images in a typical 24-hour data collection session. This should facilitate structure determination for samples with significant conformational or biochemical heterogeneity.

The second benefit is the ability to collect a "complete" dataset (i.e. of sufficient size that more data does not improve the reconstruction) in a fraction of the time currently required at most EM facilities. The fact that a single exposure on a 2-lens, 200 kV microscope can be used to determine a sub-4 Å 3D reconstruction of a particle with 6-fold symmetry should be transformative. Our results imply that ~20-100 micrograph LMSR datasets could be more than sufficient to determine high-resolution reconstructions of many well-behaved asymmetric molecules. In principle, this could allow multiple complete datasets to be collected on several different samples in a 24-hour period on a single instrument.

The choice of magnification for LMSR imaging will depend upon the desired resolution of the final reconstruction. Our results indicate that super-resolution reconstructions with resolutions ~4/3 the physical Nyquist frequency limit are possible, as we produced a 3.06 Å reconstruction when the physical Nyquist limit was 4.20 Å. Under these same imaging conditions, we obtained a 3.6 Å reconstruction with only 5 micrographs and ~13,000 particles, and a 3.72 Å reconstruction with only 1 micrograph and ~2,600 particles. Therefore, to maximize the number of particles that can be imaged while retaining the ability to generate high-resolution reconstructions with reasonable particle numbers, we suggest researchers choose a magnification resulting in a physical pixel size that is ~0.6x the desired resolution. We expect that the resolution

of reconstructions can routinely reach ~1.2x the physical Nyquist limit if super-resolution imaging is performed at lower magnifications. For example, if a ~3.0 Å resolution reconstruction is desired, we suggest super-resolution imaging with a physical pixel size of ~1.8 Å. We note that for most cryo-EM experiments involving macromolecules of unknown structure, sample preparation quality, ice thickness, and the properties of the molecule itself are the primary factors most likely to limit the achievable resolution. Furthermore, this study has been performed using the K3 detector and it is currently unclear whether similar results could be obtained with other detectors capable of super-resolution imaging.

Our suggested physical pixel size for LMSR imaging with the K3 is twice that typically used in standard practice, resulting in four times as many particles per micrograph. Correspondingly, many fewer micrographs are necessary to obtain complete datasets using LMSR imaging. Even larger pixel sizes (~2.0 - 2.4 Å) can be used if the goal is to maximize particle number and ~3.5 - 4 Å resolution reconstructions are acceptable.

One possible drawback of LMSR imaging versus imaging without super-resolution is the storage space needed for the larger super-resolution micrographs. However, the cost of data storage continues to decline, with 10TB hard drives currently costing only $300 USD. Our super-resolution movie exposures from the K3 are typically ~1.7 GB each if saved as gain-corrected images (and significantly smaller if not gain-corrected), so a typical LMSR dataset will tend to be less than 2 TB in size and the cost to store each dataset is therefore ≤ $60. Considering all the other costs associated with a cryo-EM experiment, such storage costs are not a significant extra burden. As instrument time often costs $100-$200/hour in user fees, there are strong incentives to collect as much data as possible per unit time.

Another approach that facilitates collection of large amounts of data is the use of beam-image shift (a.k.a. beam tilt or beam shift) acquisition to acquire multiple exposures per sample stage movement (Cheng et al., 2018). This is beneficial because

significant time is spent waiting for stage drift to diminish after each stage movement required to center on a new hole for image acquisition. There are two approaches to beam-image shift that have been implemented, one is to take multiple exposures (as many as 10) per hole on larger (~2 μm) holes (de la Peña et al., 2018). This is only possible on 3-condenser instruments such as the Titan Krios, in which the third lens enables the formation of a very small parallel beam. With a 2-condenser instrument like the Talos Arctica, the beam cannot be made small enough while maintaining parallel illumination to enable multiple exposures per hole. The other beam-image shift approach is to acquire single exposures from several holes per stage movement (Cheng et al., 2018). This is possible on both 2-condenser and 3-condenser instruments.

It should be straightforward to combine LMSR imaging with beam-image shift exposure acquisition at multiple holes per stage movement, resulting in imaging of nearly 1 million particles per hour (60 stage movements x 4 holes x 4000 particles/hole for small particles). Given that the image distortion effects of beam-image shift can be corrected for during imaging (Glaeser et al., 2011) or data processing (Zivanov et al., 2018), we envision that soon it will be standard practice to combine beam-image shift with the LMSR approach described here to collect unprecedented amounts of single-particle cryo-EM data using both 2-condenser and 3-condenser instruments.

Methods

Sample Preparation

Powdered urease from jack bean (*Canavalia ensiformis*) (Sigma-Aldrich #U0251) was solubilized in phosphate buffered saline (137 mM NaCl, 2.7 mM KCl, 8 mM Na2HPO4, 2 mM KH2PO) at a concentration of 0.8 mg/ml, flash frozen, and stored at -80°C. Aliquots were centrifuged at 14,000g for 10 min upon thawing to remove aggregates. 3 μl of the protein solution was applied to Quantifoil R1.2/1.3 300-mesh gold-support grids that had been glow-discharged for 80 seconds at 30 mA in a Pelco EasiGlo instrument. Grids were blotted for 2.5 seconds at 4°C and 100% humidity and immediately plunge frozen in liquid ethane using a FEI Mark IV Vitrobot. Grids for both datasets were prepared at the same time under the same conditions.

Imaging conditions

Cryo-EM data collection was performed using a Thermo Fisher Scientific Talos Arctica operated at 200 keV equipped with a Gatan K3 detector operated in counting mode with 0.5X-binning (super-resolution mode) and a Gatan BioQuantum energy filter with a slit width of 20 eV.

Microscope alignments were performed on a gold diffraction cross-grating following published procedures for a 2-condenser instrument (Herzik et al., 2017, 2019). Parallel conditions were determined in diffraction mode at the imaging magnification. Beam tilt, rotation center, objective astigmatism, and coma-free alignments were performed iteratively at the imaging magnification. A C2 aperture size was chosen so that the beam was larger than the imaging area (50 μm for 49kX and 70 μm for 39kX). The spot size was set so that the dose rate in vacuum at the detector was ~40 e^-/physical pixel/sec. A 100 μm objective aperture was used during data collection.

SerialEM (Mastronarde, 2005; Schorb et al., 2019) was used for automated data collection of fractionated exposures (movies). The record settings were set to capture a total dose of ~24 $e^-/Å^2$ for the 49kX dataset or ~45 $e^-/Å^2$ for the 39kX dataset, and fractionated so that the dose per frame was ~0.8 – 0.9 $e^-/Å^2$. Dose rates on the detector while imaging the samples were ~25-30 e-/physical pixel/second.

Data Processing

All cryo-EM data processing was performed within Relion 3.0 (Zivanov et al., 2018), and software was maintained by SBGrid (Morin et al., 2013). All 3D refinements and 3D-classifications imposed D3 symmetry (six asymmetric units per molecule). Chimera (Pettersen et al., 2004) was used for visualization of reconstructions and determination of the threshold values used to create masks.

49kX magnification (physical pixel size of 1.66 Å): Frames from 240 movies were aligned and dose-weighted with MotionCor2 (Zheng et al., 2017) using 30 (6x5) patches, the default B-factor of 150, and no binning. Defocus values were calculated for the non-dose-weighted micrographs with GCTF (Zhang, 2016). 147 particles were manually picked from 6 micrographs and 2D classified to generate 4 templates for autopicking. 11,000 particles were autopicked from 16 micrographs and subjected to 3D-refinement to produce an initial 5.7 Å reconstruction, using the crystal structure of urease, PDB: 3LA4 (Balasubramanian and Ponnuraj, 2010), lowpass-filtered to 60 Å as a reference model. This reconstruction was then used as a 3D template for autopicking the entire dataset. 358,703 particles from all 240 dose-weighted, motion-corrected micrographs were extracted and binned 2x to the physical pixel size of 1.66 Å, then subjected to 3D refinement resulting in a reconstruction with a masked 0.143 FSC resolution of 3.32 Å (see Figure S1 for FSC curve). The aligned particle images were then re-extracted using the unbinned super-resolution pixel size of 0.83 Å. 3D-refinement of this unbinned particle set produced a reconstruction with a masked 0.143 FSC resolution of 3.1 Å, surpassing the physical pixel Nyquist limit of 3.32 Å. The data was then CTF refined (per-particle defocus estimation), Bayesian polished, and subjected to 3D-classification (k=3) keeping alignments fixed. The best class contained 128,947 particles and after 3D refinement produced a 2.8Å resolution reconstruction. A second round of CTF refinement, 3D-classification, and 3D-refinement resulted in a final reconstruction containing 56,038 particles with a masked 0.143 FSC resolution of 2.77 Å. See Figure S1 for a graphical flowchart of the data processing steps.

39kX magnification (physical pixel size of 2.10 Å): Frames from 284 movies were aligned and dose-weighted with MotionCor2 (Zheng et al., 2017) using the unbinned super-resolution pixel size and 30 (6x5) patches. Defocus values were estimated by CTF-fitting the non-dose-weighted micrographs with GCTF (Zhang, 2016) using information up to a resolution limit of 12 Å (using the argument "--resH 12"). 21 micrographs with GCTF maximum resolution estimates worse than 6 Å were discarded. 972,576 particles were picked from the resulting 263 micrographs using LoG autopicking in Relion. The selected particle images were extracted with a binned pixel size of 2.58 Å and 2D-classified to remove junk particles. All 2D classes that appeared to contain at least some good particles were selected resulting in 845,377 particles in 21 classes. The selected particles were refined to a generate a 3D reconstruction with resolution of 5.16 Å. Per-particle CTF refinement was then performed and the particle images were re-extracted with an unbinned super-resolution pixel size of 1.05 Å. 3D-classification with alignments was performed to reduce the number of particles in order to speed data processing. The resulting classes were essentially indistinguishable. A class of 299,603 particles was subjected to iterative rounds of 3D refinement and CTF refinement until the masked 0.143 FSC resolution converged at 3.19 Å. The output was then 3D-classified without alignments producing a class containing 111,111 particles that after an additional round of 3D refinement yielded no further improvement. Subsequent Bayesian particle polishing and 3D refinement resulted in a final reconstruction with a masked 0.143 FSC resolution of 3.06 Å. Further attempts at 3D classification and CTF refinement did not improve the resolution. See Figure S2 for a graphical flowchart of the data processing steps.

20 micrograph 39kX magnification dataset: 78,970 unbinned autopicked particles were extracted from the first 20 micrographs of the 39kX magnification dataset. Using an approach similar to that described above, 41,938 particles were used to generate a 3D reconstruction with a final masked 0.143 FSC resolution of 3.34 Å.

5 micrograph 39kX magnification dataset: 19,964 unbinned autopicked particles were extracted from the first 5 micrographs of the 39kX magnification dataset. Using an approach similar to that described above, 12,582 particles were used to generate a 3D reconstruction with a final masked 0.143 FSC resolution of 3.60 Å.

Single exposure: Initially, the two micrographs with the lowest estimated defocus values (approximately 0.8 μm and 0.9 μm underfocus) displaying good contrast among the first 20 micrographs of the 39kX magnification dataset were selected and processed independently using an approach similar to that described above. From the 0.9 μm underfocus micrograph, 3,912 particles were autopicked and processed to generate a 3D-reconstruction with a masked 0.143 FSC resolution of 3.84 Å using 2,967 particles selected after 3D classification. From the 0.8 μm underfocus micrograph, 3,830 particles were autopicked and processed to generate a selected after 3D-reconstruction with a masked 0.143 FSC resolution of 4.12 Å using 3,160 particles selected after 3D classification. Subsequently, we chose three more single exposures to process in a similar manner. See Figure S3 for a graphical flowchart of the data processing steps leading to the 3.84 Å reconstruction.

Atomic model building and real-space refinement

The final sharpened masked electron density map was used to build an atomic model of jack bean urease by modifying the crystal structure (Balasubramanian and Ponnuraj, 2010) in Coot (Emsley and Cowtan, 2004; Emsley et al., 2010). Real-space refinement (Afonine et al., 2018b) was performed and validated in Phenix (Moriarty et al., 2009; Adams et al., 2010; Afonine et al., 2018a; Williams et al., 2018) using the same map. Hydrogen atoms were included during refinement but removed from the models prior to final validation. We used “map-to-model” (Terwilliger et al., 2018) and “chain comparison” within Phenix to determine the fraction of urease residues that could be successfully modeled automatically. Figures depicting atomic models and electron density were generated with PyMol.

Determination of the MTF, NPS, and DQE of the K3 detector

We collected super-resolution images of the imaging-filter knife-edge aperture at varying dose rates. At each dose rate we collected two equal exposures using an exposure time sufficient to result in a total dose of ~250 e^-/physical pixel (~62.5 e^-/super-resolution pixel). We then used FindDQE (version 19-05-28_6100) (Ruskin et al., 2013) to generate the MTF, NPS, and DQE curves.

MTF curves, scaled to either fractional physical Nyquist or fractional super-Nyquist frequencies, have been formatted as .star files for use in RELION post-processing calculations and are available upon request.

Data and model deposition

3D-reconstructions have been deposited in the EMDB and will be released upon publication: 49kX reconstruction, EMD-20016; 39kX reconstruction, EMD-20213; single-micrograph reconstruction, EMD-20214. The 2.77 Å atomic model of urease will be deposited in the RCSB database and released upon publication. Raw movie files will be deposited in the EMPIAR database and released upon publication.

Acknowledgements

We thank Niko Grigorieff for sharing the latest version of FindDQE and for providing very helpful advice regarding its use. We thank Lena Kourkoutis and Mariena Silvestry-Ramos for critical reading of the manuscript. This work was supported by NIH/NIGMS grants R01GM098621 and R01GM116942 to J.C.F and NIH training grant T32GM007273 to J.R.F. This work made use of the Cornell Center for Materials Research (CCMR) Shared Facilities which are supported through the NSF MRSEC program (DMR-1719875). We thank the Cornell University Office of the Provost for funding the acquisition and maintenance of the microscope, and CCMR staff for advice and support.

Table 1: Estimated number of particles per micrograph at different magnifications

Nominal Magnification	Detector	Image Physical Pixel Size	Physical Nyquist	Super-Nyquist	Mag detector area	~particles / micrograph
79kX	K2	1.03 Å	2.06 Å	1.03 Å	15.1 million Å^2	400
63kX	K2	1.29 Å	2.58 Å	1.29 Å	23.7 million Å^2	630
79kX	K3	1.03 Å	2.06 Å	1.03 Å	25.0 million Å^2	660
63kX	K3	1.29 Å	2.58 Å	1.29 Å	39.2 million Å^2	1000
49kX	K3	1.66 Å	3.32 Å	1.66 Å	64.9 million Å^2	1700
39kX	K3	2.10 Å	4.20 Å	2.10 Å	103.9 million Å^2	2750

The "~particles / micrograph" numbers in this table assume a uniform sample distribution resulting in 400 particles per K2 image at 1.03 Å/pixel
The K2 detector is a 3838 x 3710 array of pixels
The K3 detector is a 5760 x 4092 array of pixels

Table 2: Datasets and reconstructions

Nominal Magnification	Detector	Physical Nyquist	Super-Nyquist	Micrographs	Total Particles	Final Particles	0.143 FSC (masked)
49kX	K3	3.32 Å	1.66 Å	240	358,703	56,038	2.77 Å
39kX	K3	4.20 Å	2.10 Å	284	972,576	111,111	3.06 Å
39kX	K3	4.20 Å	2.10 Å	20	78,970	41,938	3.34 Å
39kX	K3	4.20 Å	2.10 Å	5	19,964	12,582	3.60 Å
39kX	K3	4.20 Å	2.10 Å	1	3,912	2,967	3.84 Å
39kX	K3	4.20 Å	2.10 Å	1	3,860	2,072	4.05 Å
39kX	K3	4.20 Å	2.10 Å	1	3,267	2,998	3.98 Å
39kX	K3	4.20 Å	2.10 Å	1	3,830	3,160	4.12 Å
39kX	K3	4.20 Å	2.10 Å	1	3,540	2,588	3.72 Å

Table 3: Atomic model statistics

Imaging conditions			
Nominal magnification:	49kX	39kX	39kX
Physical pixel size:	1.66 Å	2.10 Å	2.10 Å
Super-res pixel size:	0.83 Å	1.05 Å	1.05 Å
Micrographs in dataset:	240	260	1
Particles used for final model:	56,038	111,111	2,967
0.143 FSC (masked):	2.77 Å	3.06 Å	3.84 Å
Model-map 0.5 FSC:	2.9 Å	3.1 Å	3.8 Å
Model-map masked CC	0.89	0.84	0.83
Ramachandran plot (%)			
Favored	93.41	97.17	92.97
Allowed	6.59	2.83	7.03
Outliers	0.00	0.00	0.04
Clash score	5.99	5.00	8.45
Bonds (RMSD)			
Length (Å)	0.021	0.004	0.005
Angles (°)	0.968	0.593	0.699
Rotamer outliers (%)	0.12	0.00	0.00
MolProbity score	1.76	1.41	1.91
Map-to-model automated building			
Close (%)	95.1	93.8	50.9
Matching sequence (%)	55.2	44.9	8.0

Figure Legends

Figure 1: Magnification, MTF, NPS, and DQE of the K3 detector

A) An image of a R1.2/1.3 Quantifoil hole with depicted imaging areas captured by the K3 detector at the indicated magnified image pixel sizes. Note, the actual hole diameter is ~1.5 μm. B) MTF (modulation transfer function) of the K3 as measured at 200 kV at different indicated dose rates (electrons/physical-pixel/second). C) NPS (noise power spectrum) of the K3 as measured at 200 kV at different indicated dose rates. Smoothed curve fits are shown as solid lines. D) DQE (detective quantum efficiency) of the K3 as measured at 200 kV at different indicated dose rates. Plots shown in *B-D* were determined by FindDQE (Ruskin et al., 2013) using images of a knife-edge aperture.

Figure 2: 2.77 Å super-resolution reconstruction of jack bean urease surpasses the physical Nyquist limit of 3.32 Å

A) Example motion-corrected micrograph imaged at 49kX nominal magnification resulting in a physical pixel size of 1.66 Å and physical Nyquist limit of 3.32 Å. The width of the magnified image is 956 nm. The image has been low-pass filtered to 20 Å. B) Final sharpened reconstruction colored by local resolution. C) FSC curve for the final reconstruction particle set. The 0.143 and 0.5 FSC cutoffs are shown as dotted lines, the physical Nyquist and super-Nyquist frequencies are shown as dashed lines. D) Example electron density of the final sharpened 3D reconstruction overlaid on the atomic model.

See Figure S1 for a graphical depiction of the data processing steps.

Figure 3: 3.06 Å super-resolution reconstruction of jack bean urease surpasses the physical Nyquist limit of 4.20 Å

A) Example motion-corrected micrograph imaged at 39kX nominal magnification resulting in a physical pixel size of 2.10 Å and physical Nyquist limit of 4.20 Å. The width of the magnified image is 1,210 nm. The vertical white line is an unexplained imaging artefact. The gradient of ice thickness within the hole is visible as a contrast gradient. The edge of the hole is visible in the upper right corner of the image. The image has been low-pass filtered to 20 Å. B) Selected classes after initial 2D-classification to

remove junk particles. Individual box edge width is ~230 Å. C) Final sharpened 3D-reconstruction colored by local resolution. D) FSC curve for the final reconstruction particle set. The 0.143 and 0.5 FSC cutoffs are shown as dotted lines, the physical Nyquist and super-Nyquist frequencies are shown as dashed lines. E) Example electron density of the final sharpened 3D reconstruction overlaid on the atomic structure. See Figure S2 for a graphical depiction of the data processing steps.

Figure 4: Single micrographs produce super-resolution reconstructions

A) Final 3.84 Å sharpened reconstruction generated from a subset of the particles from the micrograph shown in Fig. 3A, colored by local resolution. B) FSC curves for the final particle sets used in 3D-reconstructions from five separate single-micrograph datasets. The 0.143 and 0.5 FSC cutoffs are shown as dotted lines, the physical Nyquist and super-Nyquist frequencies are shown as dashed lines. The curve for the particle set derived from the micrograph shown in Fig. 3A and used for the reconstruction shown in panels *A* and *B* is shown in blue. C) Example electron density of the final sharpened 3D-reconstruction overlaid on the atomic structure. D) Violin plot depicting the distribution of refined defocus U values of the particles used in the final reconstruction shown in panel *A*. E) Plot depicting the spatial distribution of refined defocus U values of the particles used in the final reconstruction shown in panel *A*. Note the presence of several particles with unrealistic defocus values calculated during CTF refinement. See Figure S3 for a graphical depiction of the data processing steps.

Figure S1: Data processing flowchart for the 49kX super-resolution dataset

See Methods for details and description.

Figure S2: Data processing flowchart for the 39kX super-resolution dataset

See Methods for details and description.

Figure S3: Data processing flowchart for the single micrograph super-resolution dataset

See Methods for details and description.

References

Adams PD, Afonine PV, Bunkoczi G, Chen VB, Davis IW, Echols N, Headd JJ, Hung LW, Kapral GJ, Grosse-Kunstleve RW, McCoy AJ, Moriarty NW, Oeffner R, Read RJ, Richardson DC, Richardson JS, Terwilliger TC, Zwart PH. 2010. PHENIX: a comprehensive Python-based system for macromolecular structure solution. *Acta Crystallogr D Biol Crystallogr* **66**:213–221. doi:S0907444909052925 [pii]10.1107/S0907444909052925

Afonine PV, Klaholz BP, Moriarty NW, Poon BK, Sobolev OV, Terwilliger TC, Adams PD, Urzhumtsev A. 2018a. New tools for the analysis and validation of cryo-EM maps and atomic models. *Acta Crystallogr D Struct Biol* **74**:814–840. doi:10.1107/S2059798318009324

Afonine PV, Poon BK, Read RJ, Sobolev OV, Terwilliger TC, Urzhumtsev A, Adams PD. 2018b. Real-space refinement in PHENIX for cryo-EM and crystallography. *Acta Crystallogr D Struct Biol* **74**:531–544. doi:10.1107/S2059798318006551

Balasubramanian A, Ponnuraj K. 2010. Crystal Structure of the First Plant Urease from Jack Bean: 83 Years of Journey from Its First Crystal to Molecular Structure. *Journal of Molecular Biology* **400**:274–283. doi:10.1016/j.jmb.2010.05.009

Bammes BE, Rochat RH, Jakana J, Chen D-H, Chiu W. 2012. Direct electron detection yields cryo-EM reconstructions at resolutions beyond 3/4 Nyquist frequency. *J Struct Biol* **177**:589–601. doi:10.1016/j.jsb.2012.01.008

Booth C. 2012. K2: A Super-Resolution Electron Counting Direct Detection Camera for Cryo-EM. *Microscopy and Microanalysis* **18**:78–79. doi:10.1017/S1431927612002243

Campbell MG, Cheng A, Brilot AF, Moeller A, Lyumkis D, Veesler D, Pan J, Harrison SC, Potter CS, Carragher B, Grigorieff N. 2012. Movies of ice-embedded particles enhance resolution in electron cryo-microscopy. *Structure* **20**:1823–1828. doi:10.1016/j.str.2012.08.026

Cheng A, Eng ET, Alink L, Rice WJ, Jordan KD, Kim LY, Potter CS, Carragher B. 2018. High resolution single particle cryo-electron microscopy using beam-image shift. *Journal of Structural Biology* **204**:270–275. doi:10.1016/j.jsb.2018.07.015

Cheng A, Tan YZ, Dandey VP, Potter CS, Carragher B. 2016. Strategies for Automated CryoEM Data Collection Using Direct Detectors. *Meth Enzymol* **579**:87–102. doi:10.1016/bs.mie.2016.04.008

Cheng Y. 2015. Single-Particle Cryo-EM at Crystallographic Resolution. *Cell* **161**:450–457. doi:10.1016/j.cell.2015.03.049

Cheng Y, Grigorieff N, Penczek PA, Walz T. 2015. A primer to single-particle cryo-electron microscopy. *Cell* **161**:438–449. doi:10.1016/j.cell.2015.03.050

Chiu P-L, Li X, Li Z, Beckett B, Brilot AF, Grigorieff N, Agard DA, Cheng Y, Walz T. 2015. Evaluation of super-resolution performance of the K2 electron-counting camera using 2D crystals of aquaporin-0. *J Struct Biol* **192**:163–173. doi:10.1016/j.jsb.2015.08.015

de la Peña AH, Goodall EA, Gates SN, Lander GC, Martin A. 2018. Substrate-engaged 26S proteasome structures reveal mechanisms for ATP-hydrolysis-driven translocation. *Science* **362**. doi:10.1126/science.aav0725

Emsley P, Cowtan K. 2004. Coot: model-building tools for molecular graphics. *Acta Cryst D* **60**:2126–2132. doi:10.1107/S0907444904019158

Emsley P, Lohkamp B, Scott WG, Cowtan K. 2010. Features and development of Coot. *Acta Crystallogr D Biol Crystallogr* **66**:486–501. doi:S0907444910007493 [pii]10.1107/S0907444910007493

Glaeser RM, Typke D, Tiemeijer PC, Pulokas J, Cheng A. 2011. Precise beam-tilt alignment and collimation are required to minimize the phase error associated with coma in high-resolution cryo-EM. *Journal of Structural Biology* **174**:1–10. doi:10.1016/j.jsb.2010.12.005

Herzik MA, Wu M, Lander GC. 2019. High-resolution structure determination of sub-100 kDa complexes using conventional cryo-EM. *Nat Commun* **10**:1032. doi:10.1038/s41467-019-08991-8

Herzik MA, Wu M, Lander GC. 2017. Achieving better-than-3-Å resolution by single-particle cryo-EM at 200 keV. *Nat Methods* **14**:1075–1078. doi:10.1038/nmeth.4461

Li X, Mooney P, Zheng S, Booth CR, Braunfeld MB, Gubbens S, Agard DA, Cheng Y. 2013a. Electron counting and beam-induced motion correction enable near-atomic-resolution single-particle cryo-EM. *Nat Methods* **10**:584–590. doi:10.1038/nmeth.2472

Li X, Zheng SQ, Egami K, Agard DA, Cheng Y. 2013b. Influence of electron dose rate on electron counting images recorded with the K2 camera. *J Struct Biol* **184**:251–260. doi:10.1016/j.jsb.2013.08.005

Mastronarde DN. 2005. Automated electron microscope tomography using robust prediction of specimen movements. *J Struct Biol* **152**:36–51. doi:10.1016/j.jsb.2005.07.007

McMullan G, Faruqi AR, Clare D, Henderson R. 2014. Comparison of optimal performance at 300keV of three direct electron detectors for use in low dose

electron microscopy. *Ultramicroscopy* **147**:156–163. doi:10.1016/j.ultramic.2014.08.002

Mendez JH, Mehrani A, Randolph P, Stagg S. 2019. Throughput and Resolution with a Next Generation Direct Electron Detector. *bioRxiv* 620617. doi:10.1101/620617

Moriarty NW, Grosse-Kunstleve RW, Adams PD. 2009. electronic Ligand Builder and Optimization Workbench (eLBOW): a tool for ligand coordinate and restraint generation. *Acta Crystallogr D Biol Crystallogr* **65**:1074–1080. doi:10.1107/S0907444909029436

Morin A, Eisenbraun B, Key J, Sanschagrin PC, Timony MA, Ottaviano M, Sliz P. 2013. Cutting Edge: Collaboration gets the most out of software. *eLife*. doi:10.7554/eLife.01456

Nogales E, Scheres SHW. 2015. Cryo-EM: A Unique Tool for the Visualization of Macromolecular Complexity. *Mol Cell* **58**:677–689. doi:10.1016/j.molcel.2015.02.019

Pettersen EF, Goddard TD, Huang CC, Couch GS, Greenblatt DM, Meng EC, Ferrin TE. 2004. UCSF Chimera--a visualization system for exploratory research and analysis. *J Comput Chem* **25**:1605–1612. doi:10.1002/jcc.20084

Rosenthal PB, Henderson R. 2003. Optimal determination of particle orientation, absolute hand, and contrast loss in single-particle electron cryomicroscopy. *J Mol Biol* **333**:721–745.

Ruskin RS, Yu Z, Grigorieff N. 2013. Quantitative characterization of electron detectors for transmission electron microscopy. *J Struct Biol* **184**:385–393. doi:10.1016/j.jsb.2013.10.016

Schorb M, Haberbosch I, Hagen WJH, Schwab Y, Mastronarde DN. 2019. Software tools for automated transmission electron microscopy. *Nature Methods* 1. doi:10.1038/s41592-019-0396-9

Terwilliger TC, Adams PD, Afonine PV, Sobolev OV. 2018. A fully automatic method yielding initial models from high-resolution electron cryo-microscopy maps. *bioRxiv* 267138. doi:10.1101/267138

Williams CJ, Headd JJ, Moriarty NW, Prisant MG, Videau LL, Deis LN, Verma V, Keedy DA, Hintze BJ, Chen VB, Jain S, Lewis SM, Arendall WB, Snoeyink J, Adams PD, Lovell SC, Richardson JS, Richardson DC. 2018. MolProbity: More and better reference data for improved all-atom structure validation. *Protein Sci* **27**:293–315. doi:10.1002/pro.3330

Zhang K. 2016. Gctf: Real-time CTF determination and correction. *J Struct Biol* **193**:1–12. doi:10.1016/j.jsb.2015.11.003

Zheng SQ, Palovcak E, Armache J-P, Verba KA, Cheng Y, Agard DA. 2017. MotionCor2: anisotropic correction of beam-induced motion for improved cryo-electron microscopy. *Nat Methods* **14**:331–332. doi:10.1038/nmeth.4193

Zivanov J, Nakane T, Forsberg BO, Kimanius D, Hagen WJ, Lindahl E, Scheres SH. 2018. New tools for automated high-resolution cryo-EM structure determination in RELION-3. *Elife* **7**. doi:10.7554/eLife.42166

Zivanov J, Nakane T, Scheres SHW. 2019. A Bayesian approach to beam-induced motion correction in cryo-EM single-particle analysis. *IUCrJ* **6**:5–17. doi:10.1107/S205225251801463X

Figure 1

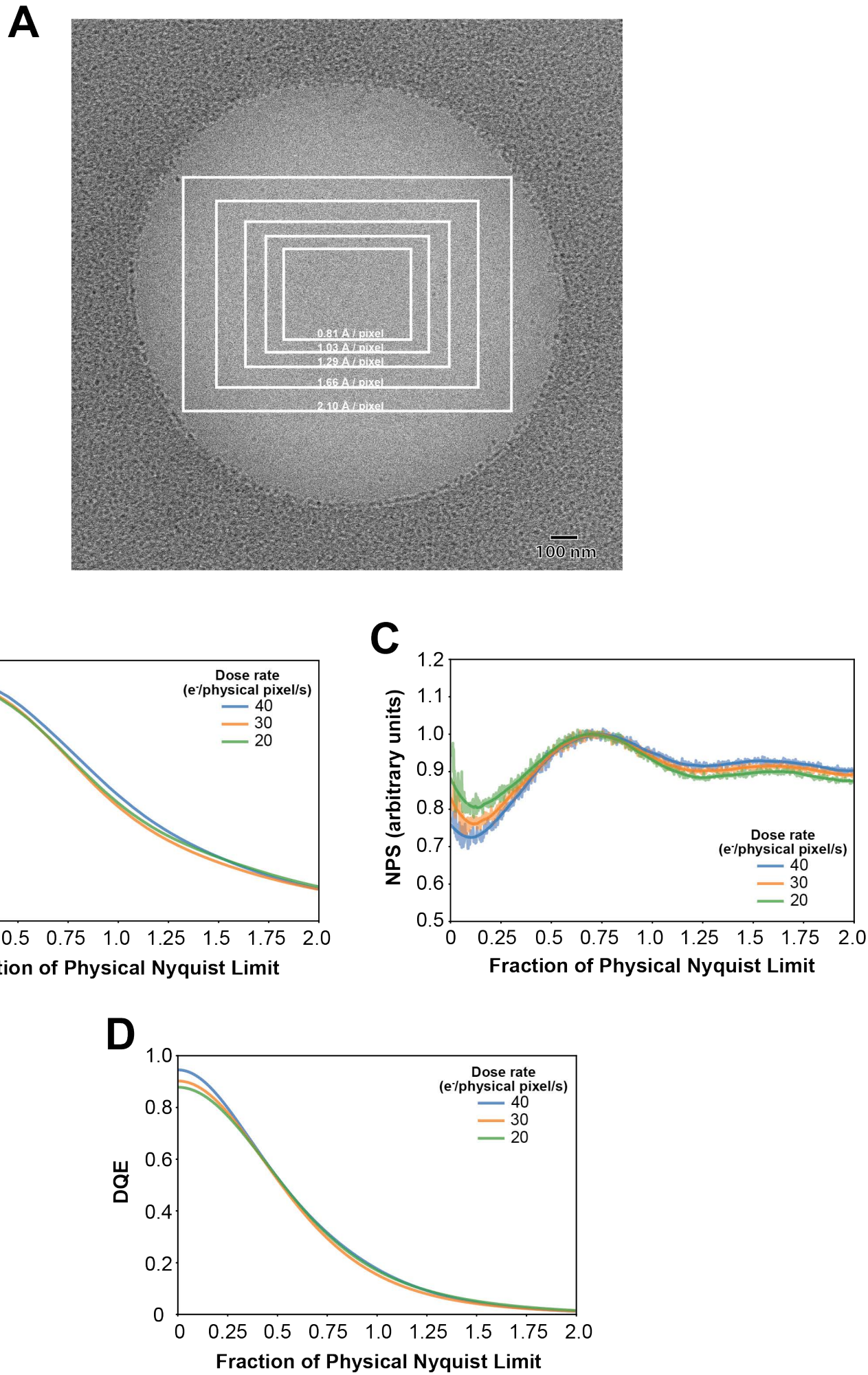

Figure 2

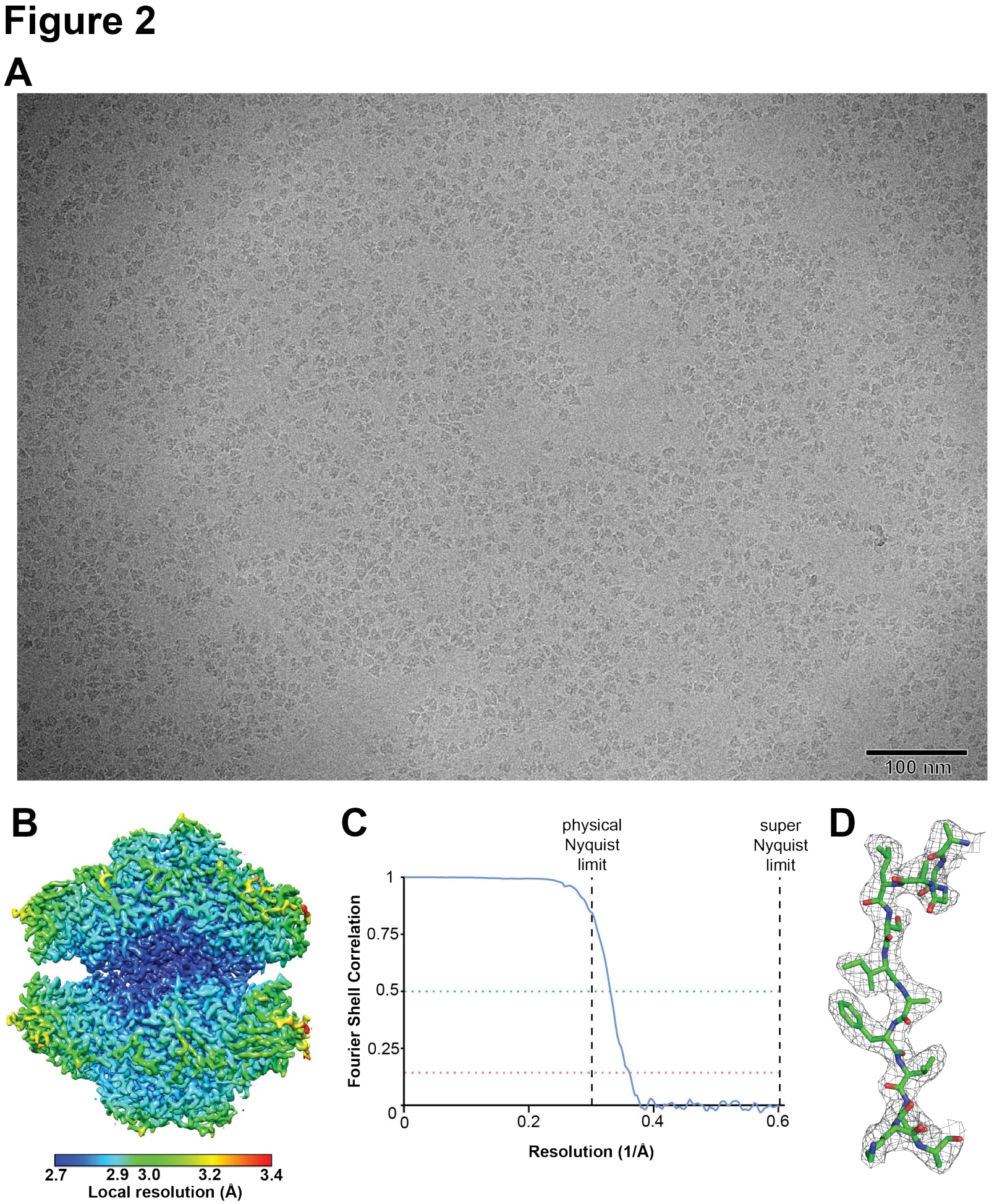
A
100 nm
B
2.7
2.9
3.0
3.2
3.4
Local resolution (Å)
C
physical
Nyquist
limit
super
Nyquist
limit
Fourier Shell Correlation
1
0.75
0.5
0.25
0
0
0.2
0.4
0.6
Resolution (1/Å)
D

Figure 3

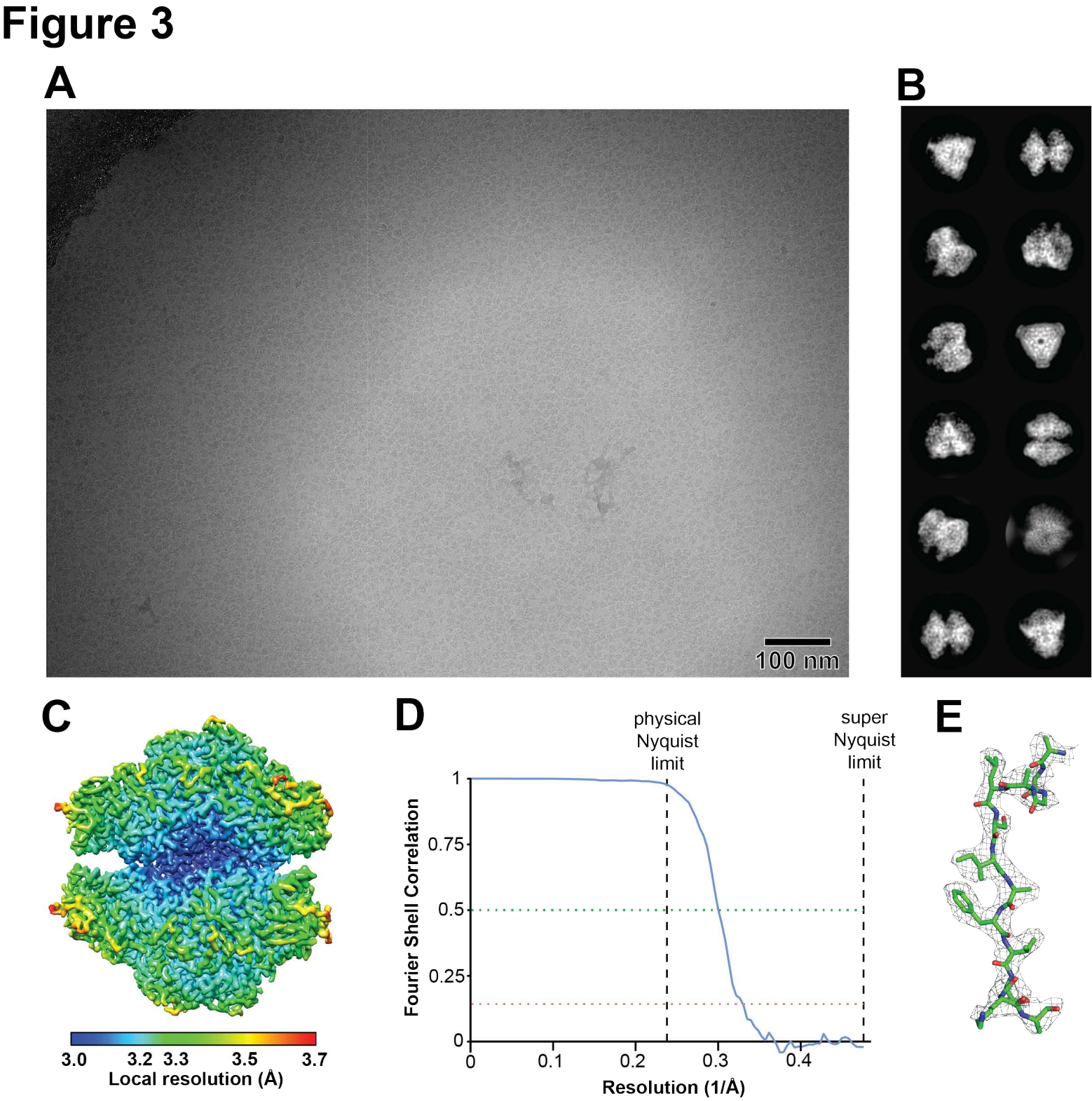
A
B
100 nm
C
3.0
3.2
3.3
3.5
3.7
Local resolution (Å)
D
physical
Nyquist
limit
super
Nyquist
limit
Fourier Shell Correlation
1
0.75
0.5
0.25
0
0
0.1
0.2
0.3
0.4
Resolution (1/Å)
E

Figure 4

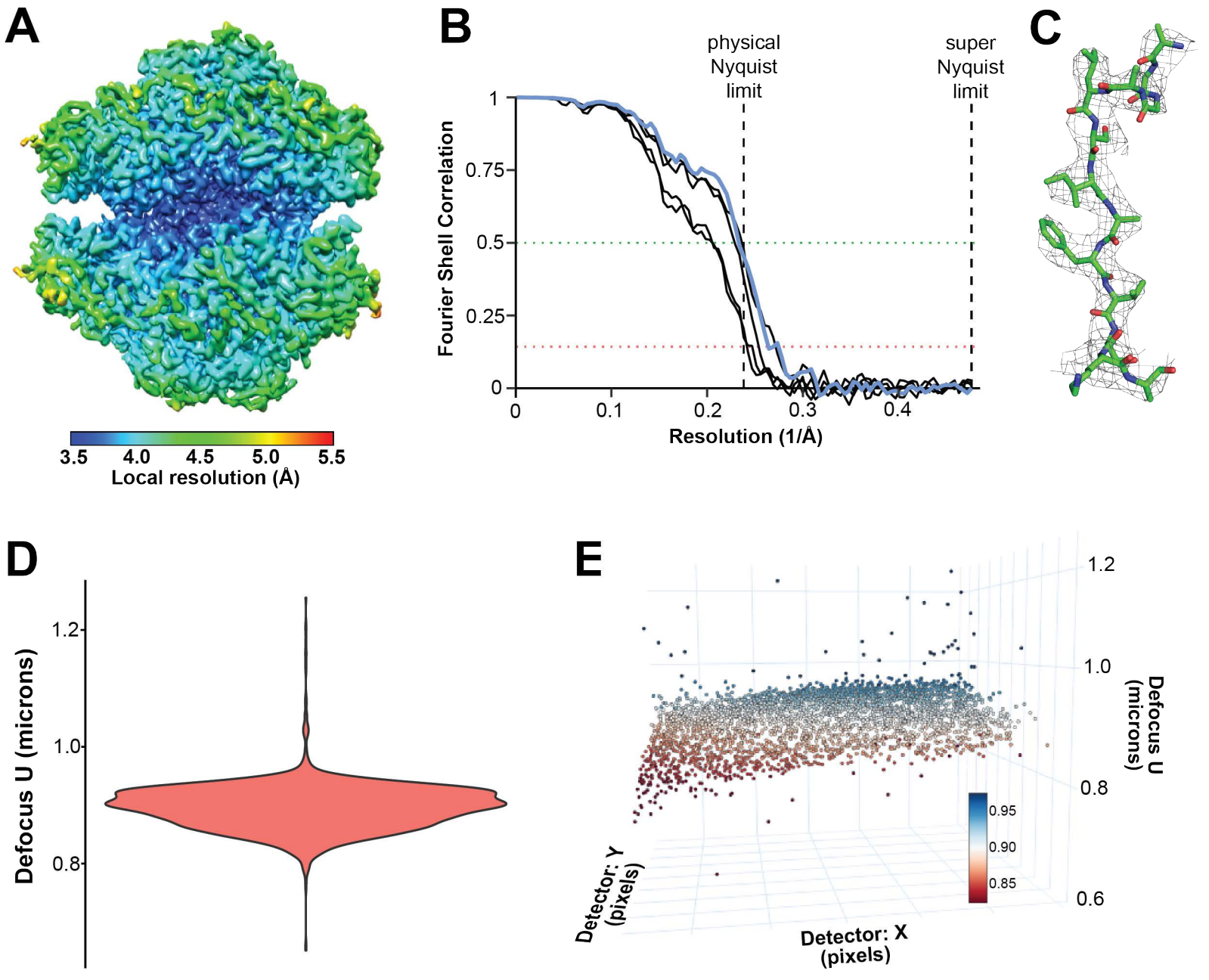
A
3.5
4.0
4.5
5.0
5.5
Local resolution (Å)
B
physical
Nyquist
limit
super
Nyquist
limit
Fourier Shell Correlation
1
0.75
0.5
0.25
0
0
0.1
0.2
0.3
0.4
Resolution (1/Å)
C
D
Defocus U (microns)
1.2
1.0
0.8
E
1.2
1.0
0.8
0.6
Defocus U
(microns)
0.95
0.90
0.85
Detector: Y
(pixels)
Detector: X
(pixels)

Figure S1

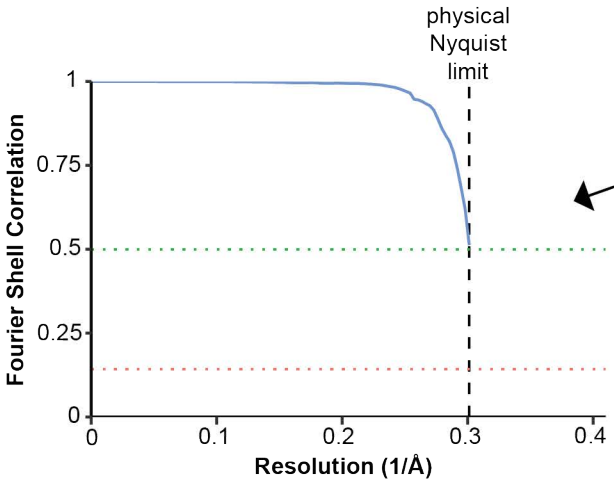

3D template autopick from
240 motion-corrected micrographs

Extract 358,703 particles
1.66 Å/pixel

3D refinement

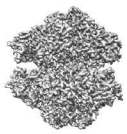

3.32Å

Re-extract 0.83 Å/pixel
3D refinement

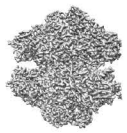

3.09 Å

Per-particle CTF refinement
3D refinement

2.87 Å

Bayesian particle polishing

3D classification, fixed alignments
Tau=8

148,149	128,948	81,607
41%	36%	23%
3.1 Å	3.0 Å	3.7 Å

3D refinement

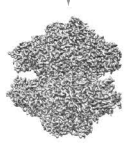

2.80 Å

Per-particle CTF refinement
3D refinement

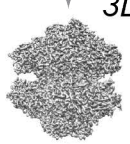

2.77 Å

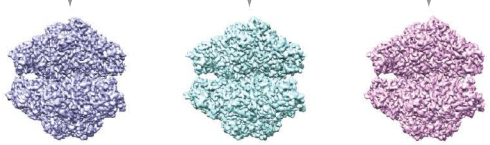

3D classification, fixed alignments
Tau=12

37,844	56,038	35,065
29%	43%	27%
3.2 Å	3.0 Å	3.2 Å

3D refinement

2.77 Å
56,038 particles

Figure S2

LoG autopick from
263 motion-corrected micrographs

Extract 972,576 Particles
2.58 Å/pixel

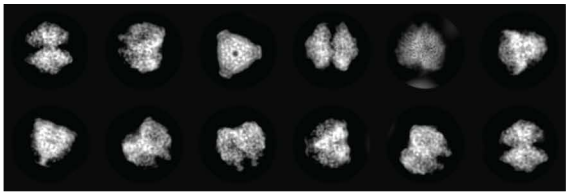

2D Classification
k = 100, Tau = 1.5, Mask = 180 Å

Select 845,377 particles
3D refinement

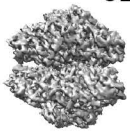

5.16 Å

Per-particle CTF refinement
Re-extract 1.05 Å/pixel

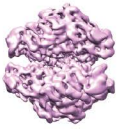

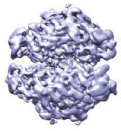

3D Classification
Tau=8

545,774
64.8%
4.36 Å

299,603
35.2%
3.98 Å

3D Refinement

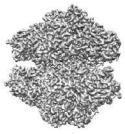

3.34 Å

2x *Per-particle CTF refinement*
3D refinement

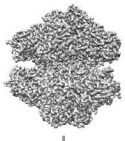

3.19 Å

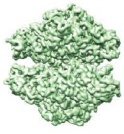

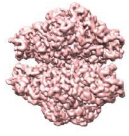

3D classification, fixed alignments
Tau=8

188,492
62.9%
3.54 Å

111,111
37.1%
3.39 Å

3D Refinement

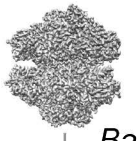

3.19 Å

Bayesian particle polishing
3D refinement

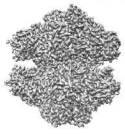

3.06 Å
111,111 particles

Figure S3

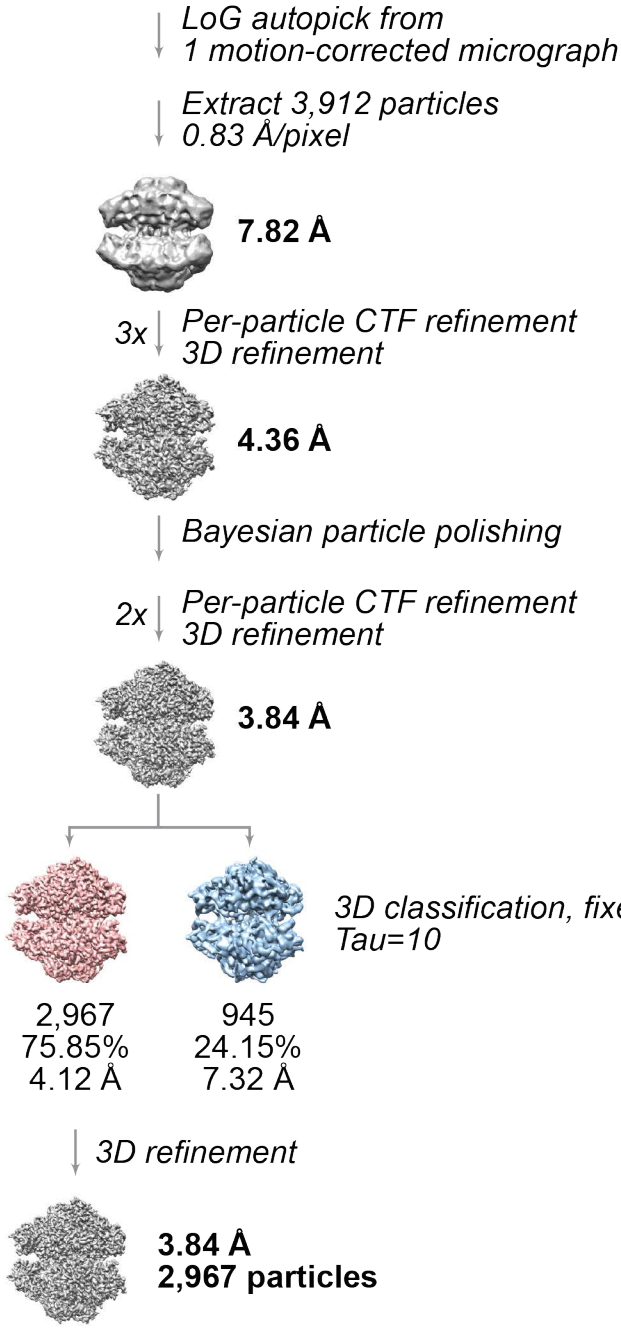
LoG autopick from
1 motion-corrected micrograph
Extract 3,912 particles
0.83 Å/pixel
7.82 Å
3x
Per-particle CTF refinement
3D refinement
4.36 Å
Bayesian particle polishing
2x
Per-particle CTF refinement
3D refinement
3.84 Å
3D classification, fixed alignments
Tau=10
2,967
75.85%
4.12 Å
945
24.15%
7.32 Å
3D refinement
3.84 Å
2,967 particles